Gate-induced half metals in Bernal-stacked graphene multilayers

Miao Liang,[1] Shuai Li,[2,*] and Jin-Hua Gao[1,†]

[1]*School of Physics and Wuhan National High Magnetic Field Center, Huazhong University of Science and Technology, Wuhan 430074, China*

[2]*Institute for Advanced Study, Soochow University, Suzhou 215006, China*

(Received 4 October 2021; revised 5 January 2022; accepted 7 January 2022; published 24 January 2022)

Recent experiments indicate that Bernal stacked graphene multilayers (BGMs) have an interaction-induced gapped (or pseudogapped) ground state. Here, we propose that, due to the electron correlation, the BGM can be induced into a half-metallic phase by applying a vertical electric field and doping. The half-metallic states in even-layer and odd-layer BGMs have totally different behaviors due to their different band structures. We systematically calculate the graphene tetralayer (4L-BGM) and trilayer (3L-BGM) as typical examples of even-layer and odd-layer BGMs, respectively. In 4L-BGMs, we find an interesting phenomenon of electric field-induced inversion of the spin-polarized bands, namely, in the half-metallic phase, the spin polarization of the conducting channel and the net magnetic moment are inversed when the applied electric field exceeds a critical value. In 3L-BGMs, a remarkable feature is that the inequivalence of the two sublattices will intrinsically break the degeneracy of the spin-up and spin-down bands even in the zero electric field case. Our results suggest that 4L-BGM could be an ideal platform to detect the proposed half-metallic phase in BGM systems.

DOI: 10.1103/PhysRevB.105.045419

I. INTRODUCTION

Graphene spintronics has drawn great research interest in the last 20 years [1–5]. The main reason is that graphene has a very long spin diffusion length of about several micrometers [4,6], which makes it an ideal platform for spin-device application. Manipulating the spin degree of freedom in graphene systems is not only of fundamental interest but also has potential device applications [7–10].

Half metal denotes a large family of materials in which electrons are conducting in one spin channel and insulating in the other [11,12]. Thus, it is natural that half-metal materials are highly attractive for spintronics applications. The conventional half-metal materials are mainly ferromagnets or ferrimagnets, e.g., Heussler alloys and transition-metal oxides [12–16].

Interestingly, though pristine graphene is not a ferromagnetic material, it was proposed that correlated half-metallic states can be realized in some graphene systems, namely, graphene nanoribbon [17–21], graphene bilayers [22], and rhombohedral stacked graphene multilayers (RGMs) [23,24], by applying a proper external electric field and doping. Such a half-metallic state can be viewed as a kind of half-metallic antiferromagnet [25–28], which results from the interplay between the interaction-induced antiferromagnetic spin order and external electric field. Take the graphene bilayer as an example. Considering the Coulomb interaction, the graphene bilayer can be described by the Hubbard model. At half filling, one of the most possible ground states is the layer antiferromagnetic (LAF) state [29–36]. The LAF state is a kind of spin density wave state, in which the spin polarization of two adjacent layers is opposite [30,37–40]. When a perpendicular electric field is applied, spin-up and spin-down electrons feel different potentials. So, the degeneracy of the spin-up bands and spin-down bands is broken. With proper tiny doping, the doped electrons are filled into just one spin-polarized band, so a half-metallic ferromagnetic state appears. The case of the RGM is the same, since it has a very similar interaction-induced antiferromagnetic spin order (LAF state) [30]. Actually, such a half-metallic state based on antiferromagnetic spin order is a general phenomenon in Hubbard lattice models [41,42]. Note that the interaction-induced half-metallic phase in rhombohedral stacked graphene trilayer has been observed in recent experiments [43,44].

It is worth noting that Bernal stacked graphene multilayers (BGMs), the most common form of graphene multilayers in nature, also have correlated ground states (gapped or pseudogapped) at low temperature, as indicated by several transport experiments on suspended samples [45–47]. Basically, there are two kinds of graphene multilayers, i.e., the RGM and the BGM, according to the stacking order. Different stacking orders give rise to different band structures. Without regard to the electron-electron interaction, an N-layer BGM is metallic, which has N parabolic bands near the Fermi level for even N and an additional Dirac cone for odd N [48–52]. Although the density of states (DOS) of BGM at E_f is not as large as that of the corresponding RGM, Coulomb interaction does induce a gap Δ_0 at zero temperature for even-layer BGM. For example, $\Delta_0 \approx 5.2$ meV for the tetralayer (4L-BGM) and $\Delta_0 \approx 13$ meV for the hexalayer (6L-BGM) [47]. The odd-layer cases have a similar phase transition as well, but the conductivity is always finite due to the additional linear bands [47].

*leeshuai@hust.edu.cn
†jinhua@hust.edu.cn

More importantly, recent first-principles calculations suggest that the correlated ground states of the BGMs also can host an antiferromagnetic spin order [53], similar to the LAF states in the RGMs. Therefore, a natural question is if the BGMs can be induced into a half-metallic ferromagnetic state via applying electric field and doping.

In this paper, based on the Hubbard model and self-consistent mean-field method, we theoretically prove that it is possible to induce a half-metallic phase in the BGMs by applying an electric field and doping. The half-metallic states in even-layer and odd-layer BGMs have rather different behaviors, which is reminiscent of the even-odd number effects reported in BGMs [49,51,52,54,55] and carbon based nanochain systems [56,57]. For even-layer BGMs, we take the 4L-BGM as an example. Similar to the case of RGMs, a vertical electric field E_0 can break the degeneracy of the spin-up and spin-down bands, and further doping is able to produce a half-metallic phase with a finite magnetic moment. Here, the spin-dependent gaps as functions of E_0 here have unique behaviors different from the RGMs, which give rise to an interesting phenomenon of inversion of the spin-polarized bands. Such spin-polarized band inversion naturally defines a critical value of electric field E_{inv}. Once $E_0 > E_{\text{inv}}$, the spin polarization of the conducting channel as well as the net magnetic moment of the half-metal is inverted. The numerical results indicate that the required doping to achieve the half-metallic states in BGM should be of the order of $10^{-10}\,\text{cm}^{-2}$, which is within the capability of the current experimental technique [46].

We then use graphene trilayers (3L-BGMs) as an example to illustrate the half-metallic phase in odd-layer BGMs. In 3L-BGMs, the half-metallic state has some special features distinct from even-layer BGMs. First, the degeneracy of the spin-up and spin-down bands are intrinsically broken without need of an external electric field. It originates from the inequivalence of the two sublattices of the odd-layer BGM, which thus should be a general feature of the Hubbard lattices with inequivalent sublattices. Second, the LAF state in 3L-BGMs is rather robust against the perpendicular electric field, so an extremely large E_0 is needed to destroy the spin order in 3L-BGMs. However, E_0 cannot obviously enlarge the split between the spin-up and spin-down bands in 3L-BGMs. It implies that the required parameter range to realize the half-metallic phase in 3L-BGMs is much narrower than that in 4L-BGMs.

According to our calculations, we suggest that the 4L-BGM could be an ideal platform to detect the predicted half-metallic phase of BGMs. A direct way is to measure the spin-resolved gap (about several meV), considering the induced net magnetic moment is much smaller than that in RGMs. Note that, very recently, ferromagnetic half-metallic states have been identified in rhombohedral stacked trilayers [43,44], and Bernal stacked bilayer graphene as well [58,59], by measuring the inverse electronic compressibility, conductance hysteresis, and giant magnetoconductance. We argue that the proposed half-metallic phase and the electric field-induced spin polarization inversion here can be detected in the same way. Our work not only reveals a fundamental and interesting feature of the correlated ground states of BGM but also enriches our understanding of the correlated half metal.

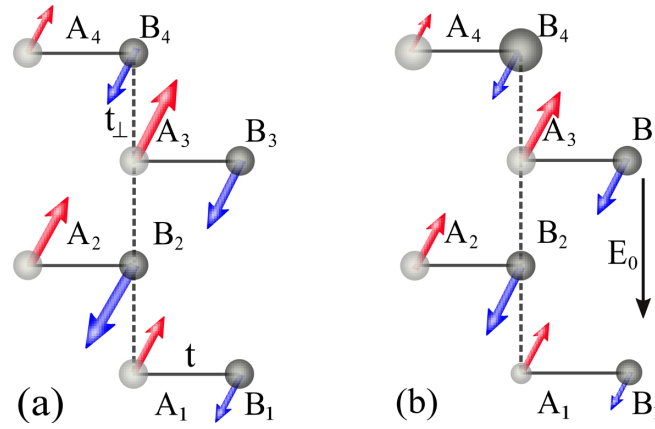

FIG. 1. Schematic diagrams of charge (sphere) and spin (arrows) structures of 4L-BGMs. (a) At half filling and in the absence of electric field. (b) At half filling and a vertical electric field E_0. A and B denote the two sublattices of graphene, and subscripts $1-4$ are layer indices. The red (blue) arrows represent up-spin (down-spin).

The paper is organized as follows. In Sec. II, we give the model and methods used in the calculations. The calculated results and corresponding discussions are given in Sec. III. Finally, we give a summary in Sec. IV.

II. MODEL AND METHODS

We use the Hubbard model and the self-consistent mean-field method to calculate the correlated ground state of the BGM. Such methods have been successfully used to describe the interaction-induced correlated states in graphene systems [22,30,60,61].

The total Hamiltonian of a given BGM is

$$H = H_0 + H_p + H_U. \tag{1}$$

Here, $H_0 = H_{\text{intra}} + H_{\text{inter}}$ is the tight-binding Hamiltonian of the BGM, and H_{intra} and H_{inter} denote the intralayer and interlayer hopping, respectively. We only include nearest-neighbor hopping in both H_{intra} and H_{inter}, where

$$H_{\text{intra}} = -t \sum_{\langle li,lj\rangle\sigma} [a^\dagger_{l\sigma}(i) b_{l\sigma}(j) + \text{ H.c. }] + \mu \sum_{li\sigma} n_{l\sigma}(i) \tag{2}$$

and

$$H_{\text{inter}} = t_\perp \sum_{\langle li,l'i'\rangle\sigma} \{a^\dagger_{l\sigma}(i) b_{l'\sigma}(i') + \text{H.c.}\}. \tag{3}$$

$a_{l\sigma}$ ($b_{l\sigma}$) is the annihilation operator of an electron on sublattice A (B). l, σ, i are the indexes of layer, spin, and site, respectively. As shown in Fig. 1, t ($t_\perp$) is the intralayer (interlayer) nearest-neighbor hopping. $\langle li, li'\rangle$ and $\langle li, l'i'\rangle$ represent the sum over all the intralayer and interlayer nearest-neighbor hoppings, respectively. For BGMs, we set $t = 3.16\,\text{eV}$ and $t_\perp = 0.381\,\text{eV}$ [22]. μ is the chemical potential and $n_{l\sigma}(i)$ is the charge density on the sites.

H_p in Eq. (1) represents the electric field induced potential,

$$H_p = \sum_{li\sigma} \Delta_l n_{l\sigma}(i), \tag{4}$$

where $\Delta_l = -eV_l$ and V_l is the potential of each layer in the presence of a vertical electric field E_0. Here, we consider the screening effect, which corresponds to a charge redistribution between layers when E_0 is applied. We define $E_l = (V_{l+1} - V_l)/d_0$ as the electric field between two adjacent layers, where l runs from 1 to $N-1$, and N is the number of layers of the system. $d_0 = 0.334$ nm is the distance between two adjacent graphene layers in BGMs. The graphene layers can be approximately viewed as conducting parallel plates. Electrostatics then tells us that

$$E_l = E_0 + 2\pi e\left[\Delta\rho_l + \sum_{l'}\Delta\rho_{l'}(2\Theta(l-l') - 1)\right], \quad (5)$$

where $\Delta\rho_l = \sum_{\sigma,i}[\langle n_{l\sigma}(i)\rangle - 1/2]/S$ is the number density of net charge in each layer and S is the area of one layer. Correspondingly, $\rho_l = \sum_{\sigma,i}\langle n_{l\sigma}(i)\rangle/S$ is the electron density in each layer. Θ is the heaviside function. Therefore, once $\langle n_{l\sigma}(i)\rangle$ are given, we can determine V_l by calculating E_l via Eq. (5), and thus get the value of Δ_l in H_p. $\langle n_{l\sigma}(i)\rangle$ is calculated in a self-consistent way, and the midpoint of the BGM along the perpendicular direction is set to be the zero potential point.

The Coulomb interaction is approximately described by the Hubbard U term. Using a mean-field approximation, we have

$$H_U^{\mathrm{MF}} = U\sum_{li\sigma}[\langle n_{l\sigma}(i)\rangle - 1/2][n_{l\bar{\sigma}}(i) - 1/2], \quad (6)$$

where $\bar{\sigma} = -\sigma$. $\langle n_{l\sigma}(i)\rangle$ has to be determined by the self-consistent method as well. The value of U is obtained by fitting the experimental value of the correlation-induced gap.

We emphasize that to stabilize the antiferromagnetic spin order, an ultradense mesh of k points is needed in the self-consistent calculation. Meanwhile, we argue that our predictions here can be further confirmed by the simulations with density functional theory [23,53].

III. RESULTS AND DISCUSSIONS

A. Half-metallic state in 4L-BGM

Taking the 4L-BGM as a typical example, we first discuss the half-metal states in the even-layer BGM. The calculated results are shown in Fig. 2.

In the single-particle picture, the 4L-BGM has two parabolic conduction bands and two parabolic valence bands touching at the Fermi level, as shown in the inset of Fig. 2(a). When the electron-electron interaction is considered, our calculation suggests that the on-site Coulomb repulsion can induce a gapped SDW-like ground state with antiferromagnetic spin order. It is in good agreement with recent DFT calculations [53]. The corresponding spin structure is shown in Fig. 1(a), where the two sublattices (A and B) have opposite spin polarization. Since the two sublattices are equivalent in 4LG-BGMs, the spin-up and spin-down bands are degenerate, as shown in Fig. 2(b). The interaction-induced gap ϵ_g depends on the value of U. As illustrated in Fig. 2(a), the larger the U, the larger the gap. In our calculations, we use $U = 6.65$ eV to fit the experimental value of the gap of 4L-BGM, i.e., $\Delta_0 \approx 5.2$ meV at zero temperature [47].

Such a correlated ground state can be viewed as a kind of LAF state. First, it has antiferromagnetic spin order, seen in Fig. 1(a), and the net spin polarization of the whole system is zero. Meanwhile, the net spin polarization in each layer is nonzero, i.e., ferrimagnetism, and that of the two adjacent layers are opposite. These features are the same as the predicted LAF states in graphene bilayers and RGMs. However, the LAF state of the BGM has its own unique features. In 4LG-BGMs, the net spin polarization mainly distribute in the inner two layers, while in RGMs the maximum value of the spin polarization occurs at the outermost two layers [30].

We then discuss the effect of the electric field in the half-filled case. An important fact is that the distributions of spin-up and -down electrons along the perpendicular direction do not coincide, as illustrated in Fig. 1(a). Thus, when a vertical electric field is applied, up spin and down spin feel the different potentials, and the degeneracy of the spin-up and -down bands is lifted. In Fig. 2(c), we see that an electric field $E_0 = 10$ mV nm^{-1} obviously decreases the gap of spin-up bands (red solid lines), while that of the spin-down band has a tiny change (blue solid lines), namely, the conduction and valence bands now are all spin-up bands. The corresponding spin and charge distributions are illustrated in Fig. 1(b). We see that the spin and charge distributions are slightly changed by the vertical electric field, but it remains in the LAF state. Very interestingly, when we use a larger electric field $E_0 = 50$ mV nm^{-1} as in Fig. 2(d), the situation reverses. The gap of spin-down bands (blue solid lines) is now suppressed instead, and becomes smaller than that of the spin-up bands. Meanwhile, due to the electric field effect, the spin-up bands change saliently from the parabolic dispersion to the Mexican hat shape. Such unique phenomenon implies that there exists an inversion of spin-polarized bands in 4L-BGMs when increasing E_0. Further increasing E_0, a transition from the LAF state to the layered charge polarized (LCP) state [22,29] occurs at the critical value $E_c = 54$ mV nm^{-1}. Then, the bands become spin degenerate, see Fig. 2(e), with $E_0 = 60$ mV nm^{-1}.

The spin-polarized band inversion is shown more clearly in Fig. 2(f), where we plot both $\epsilon_{g_\uparrow}$ (gap of spin-up bands, red lines) and $\epsilon_{g_\downarrow}$ (gap of spin-down bands, blue lines) as functions of E_0. Increasing E_0, the $\epsilon_{g_\uparrow}$ decreases at first and then increases, while the $\epsilon_{g_\downarrow}$ has the opposite behavior. The two curves have an intersection point at $E_{\mathrm{inv}} \approx 24$ mV nm^{-1}, where $\epsilon_{g_\uparrow} = \epsilon_{g_\downarrow}$. So, E_0 actually has three different regions:

(1) $E_0 < E_{\mathrm{inv}}$. In this region, $\epsilon_{g_\uparrow} < \epsilon_{g_\downarrow}$. $\epsilon_{g_\downarrow}$ first increases to a maximal value of about 6.3 meV and then decreases, while the $\epsilon_{g_\uparrow}$ first decreases to a minimal value of about 0.2 meV and then increases. The corresponding energy bands are like that in Fig. 2(c). Because both the valence and conduction bands are spin-up bands in this situation, it is in some sense can be viewed as a half semiconductor.

(2) $E_{\mathrm{inv}} < E_0 < E_c$. In this region, $\epsilon_{g_\downarrow} < \epsilon_{g_\uparrow}$. The energy bands in this region are like that in Fig. 2(d). Now, it is still in the half semiconductor state but both the valence and conduction bands are spin-down bands. Note that the spin-up bands have been changed to a Mexican hat shape.

(3) $E_0 > E_c$. In this region, the bands become spin degenerate, see Fig. 2(e). It indicates a phase transition from the LAF to the LCP state. As E_0 increases further, the gap increases monotonously.

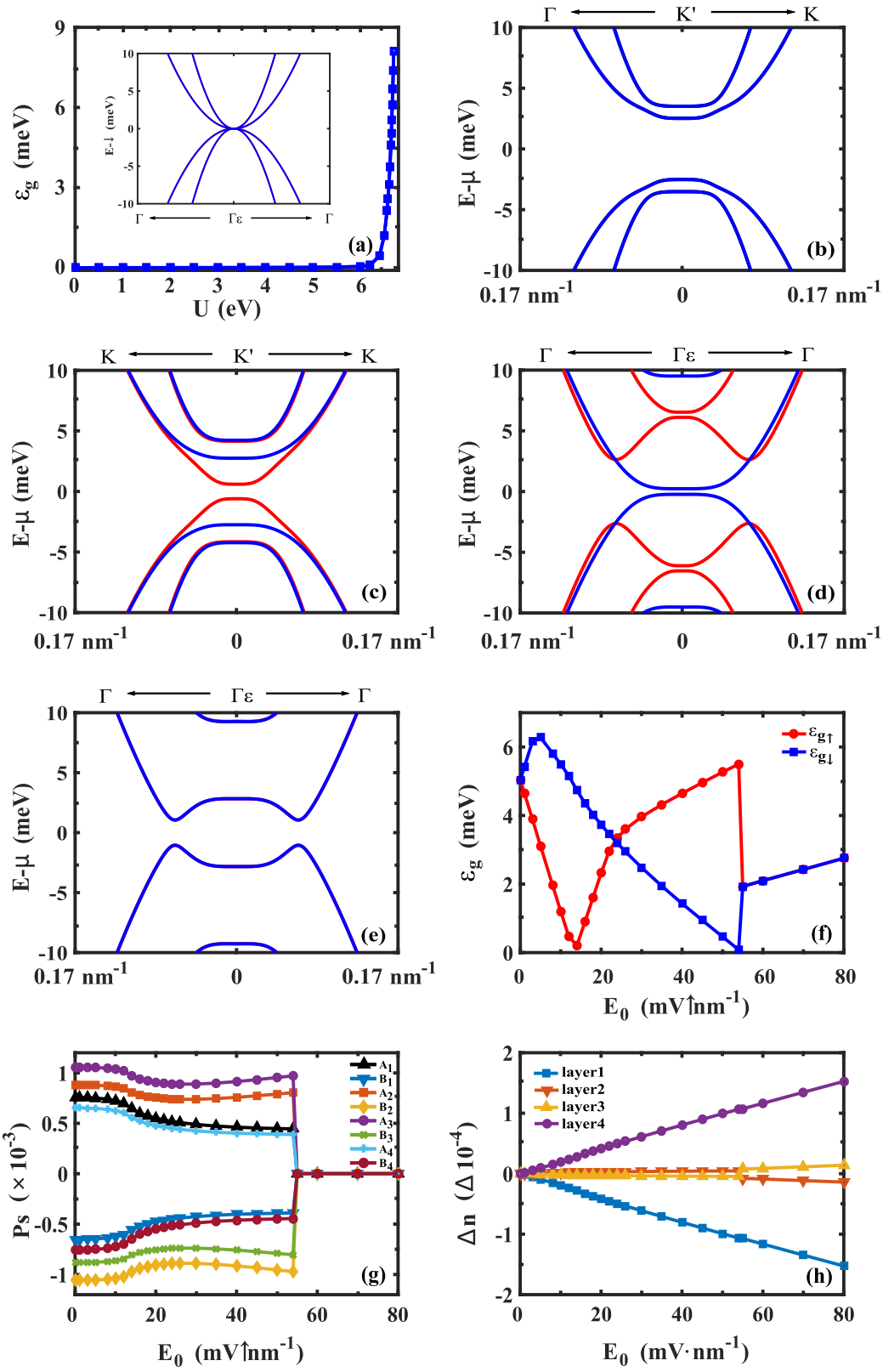

FIG. 2. 4L-BGM at half filling. (a) Energy gap of 4L-BGM as a function of U and in the absence of E_0. Insets: Low-energy bands with $U = 0$. (b) Low-energy bands with $U = 6.65$ eV, $t = 3.16$ eV, and $t_\perp = 0.381$ eV. The following (c)–(e) use the same parameters as that in (b). (c) and (d) show energy bands of the LAF stateS at (c) $E_0 = 10$ mV nm^{-1} and (d) $E_0 = 50$ mV nm^{-1}, respectively. Red (blue) solid lines denote energy bands for spin-up (down) channels. (e) Energy bands of the LCP state in 4L-BGMs with $E_0 = 60$ mV nm^{-1}. (f) Spin-resolved energy gaps against electric field E_0. (g) Spin polarization P_s at each site in the unit cell as a function of E_0. (h) The charge variation Δn on each layer as a function of E_0.

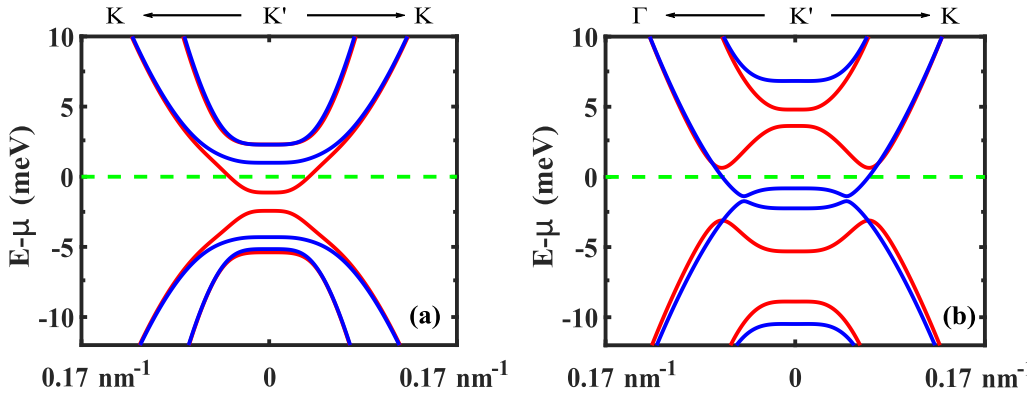

FIG. 3. Half-metallic phases in 4L-BGM. (a) Energy bands of the half-metallic phase with an up-polarized net magnetic moment. The charge density is $\delta n \approx 2.21 \times 10^{10}$ cm^{-2} and other parameters are the same as that in Fig. 2(c). (b) Energy bands of the half-metallic state with a down-polarized net magnetic moment. The charge density is $\delta n \approx 6.28 \times 10^{10}$ cm^{-2} and the parameters used are the same as Fig. 2(d). The Fermi level E_f is set at zero energy and is represented by the green horizontal dashed lines.

We emphasize that the electric field-induced spin-polarized band inversion is a unique feature of the 4L-BGM, which is distinct from that in graphene bilayers or RGMs. In graphene bilayers, as E_0 increases, the gap of one spin increases and that of the other spin decreases until E_0 exceeds a critical value and the phase transition occurs [22], namely, there is no such spin-polarized band inversion in graphene bilayers and RGMs.

In Fig. 2(g), we plot the spin polarization P_s on each site as a function of E_0, in which the phase transition at E_c is shown very clearly. We also plot the charge variation Δn on each layer as a function of E_0 in Fig. 2(h). It indicates that, as E_0 increases, an obvious charge transfer from the bottom layer (layer 1) to the top layer (layer 4) occurs. Meanwhile, the charge on the middle two layers is nearly invariant.

In the cases of graphene bilayers and RGMs, we can get a half-metal state by slightly doping the LAF state in the presence of E_0. A similar mechanism is also valid for the 4L-BGMs. Tiny doping can shift the Fermi level and partially fill the spin-polarized conduction (or valence) band of the LAF state, which gives rise to a half-metallic phase. However, as mentioned above, the 4L-BGM has two different LAF states with different E_0, where the spin polarization of the conduction and valence bands are opposite. Therefore, the 4L-BGM has two half metal regions, as shown in Fig. 3, whose net magnetic moments have opposite directions. In Fig. 3(a), the charge density is about $\delta n \approx 2.21 \times 10^{10}\,\mathrm{cm}^{-2}$ with $E_0 = 10\,\mathrm{mV\,nm}^{-1}$, while the charge density is $\delta n \approx 6.28 \times 10^{10}\,\mathrm{cm}^{-2}$ in Fig. 3(b) with $E_0 = 50\,\mathrm{mV\,nm}^{-1}$. Apparently, the conducting channels in Figs. 3(a) and 3(b) have opposite spin polarizations. Larger doping will directly destroy the LAF states and thus kill the half-metallic phase. For example, doping about $\delta n \approx 1.7 \times 10^{11}\,\mathrm{cm}^{-2}$ is large enough to kill the half-metallic phase of 4L-BGMs.

The induced magnetic moment and the spin-resolved gap are two markers of the half-metallic phase in 4L-BGMs. Since the net magnetic moment is zero at half filling, only the doped electrons contribute to the net magnetic moment, see Fig. 3. So, the magnetic moment density of the half-metallic phase in 4L-BGMs should be of the order of $10^{10}\mu_B$ cm^{-2}. Meanwhile, we argue that transport experiments to measure the spin-resolved gap (about several meV as shown in Figs. 2 and 3) is also a feasible way to identify the half-metallic phase. Considering that the correlated half-metallic phase in rhombohedral stacked graphene trilayers has been observed in experiments very recently [43,44], we expect that the proposed half-metallic phase in 4L-BGMs can be confirmed in future experiments.

In the above, we consider the half-metal phase in 4L-BGMs. Other even-layer BGMs have similar single-particle band structures, i.e., parabolic bands touching at the Fermi level. Meanwhile, the interaction-induced correlated ground state has also been observed in the Bernal stacked graphene hexalayer (i.e., 6L-BGM) in experiments [47]. Thus, it is natural to expect that 6L-BGMs can also have a half-metallic state like that in 4L-BGMs. We calculate the case of 6L-BGMs as well, and the results are quite like the case of 4L-BGMs. The 6L-BGM does have a half-metallic phase in the presence of a vertical electric field and tiny doping, and the similar electric field-induced spin-polarized band inversion has also been observed.

We argue that such a correlated half-metallic state is a general phenomenon of the even-layer BGM, as long as it has a LAF-like ground state. Note that the LAF state has been observed in all even-layer BGMs up to 8L-BGMs [45,47].

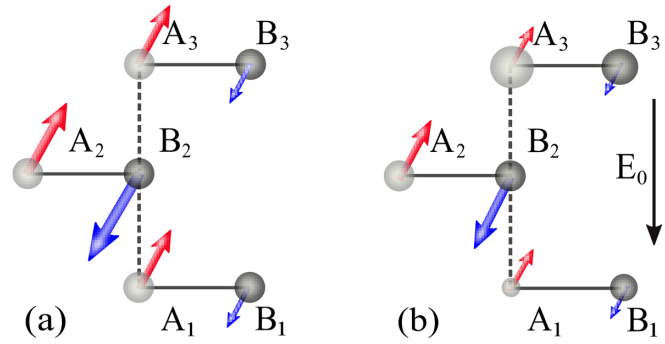

FIG. 4. Schematic illustration of the charge (sphere) and spin (arrows) structures of 3L-BGMs. (a) At half filling and in the absence of electric field. (b) At half filling and a finite perpendicular electric field E_0.

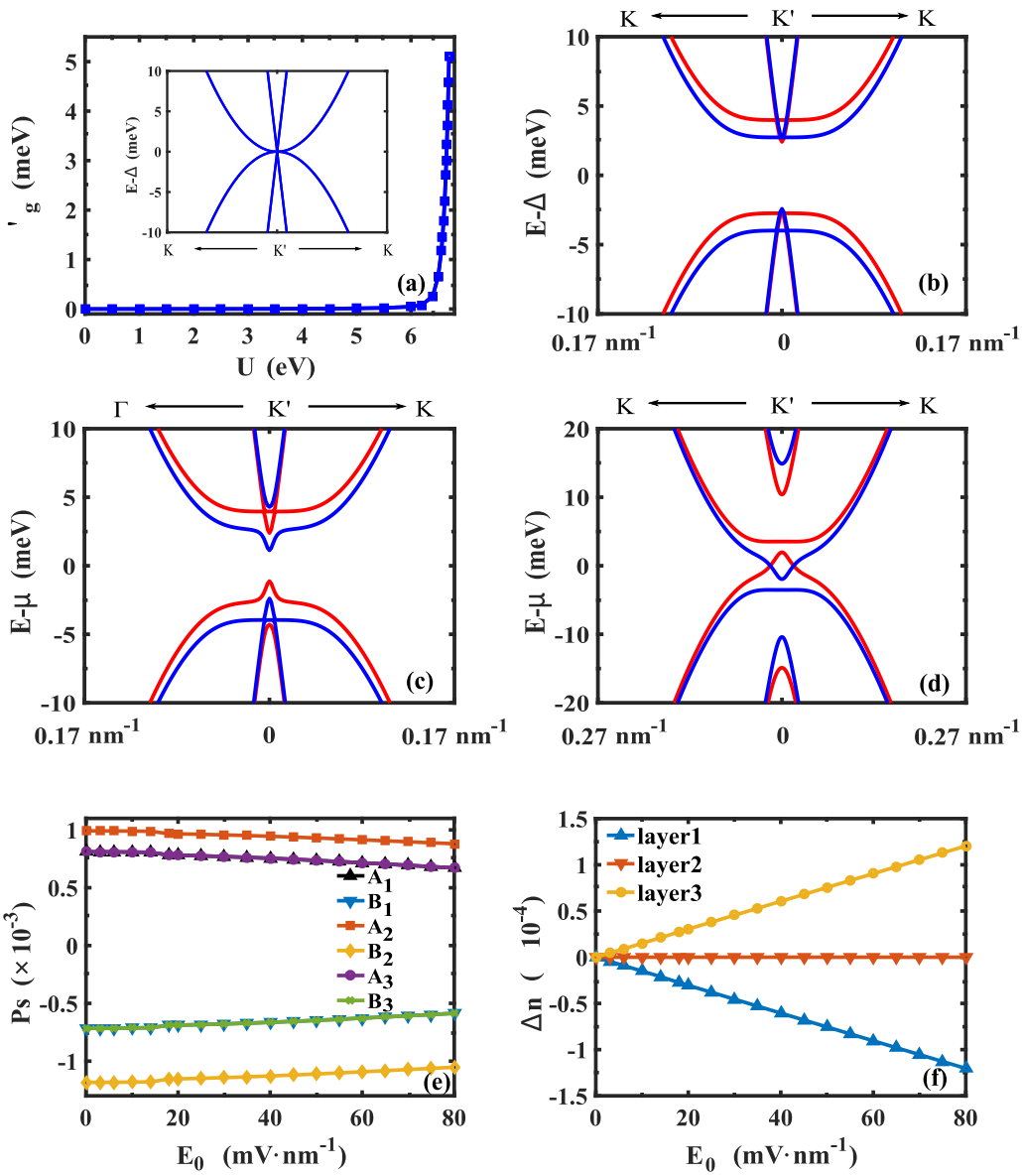

FIG. 5. 3L-BGM at half filling. (a) Energy gap of 3L-BGM as a function of U and in the absence of E_0. Inset shows the low-energy bands with $U = 0$. (b) Low-energy bands with parameters $U = 6.70\,\text{eV}$, $t = 3.16\,\text{eV}$, and $t_\perp = 0.381\,\text{eV}$. The following (c) and (d) use the same parameters of (b). (c) and (d) show the energy bands of the LAF states at the electric field (c) $E_0 = 10\,\text{mV}\,\text{nm}^{-1}$ (d) $E_0 = 80\,\text{mV}\,\text{nm}^{-1}$. (e) Spin polarization P_s at each site in the unit cell as a function E_0. (f) The charge variation Δn on each layer versus E_0.

Thus, a conservative statement is that, at least, the proposed half-metallic phase can be observed in all even-layer BGMs up to 8L-BGMs. However, there should be an up limit of the thickness of BGMs, above which the half-metallic phase does not occur. It is because when the thickness of the BGM increases, it will approach graphite, which does not support the LAF states. Since in our calculation the Hubbard U term is obtained by fitting the experiment, we can not directly predict the up limit of thickness here. We think it can be estimated via first-principles simulations.

B. Half-metallic state in 3L-BGM

Former DFT calculations [53] reported that odd-layer BGMs, like graphene trilayers (i.e., 3L-BGMs), can also host a stable LAF state as illustrated in Fig. 4, though its conductance is always finite (pseudogapped) [47]. Here we calculate the electric field effects on the LAF state in 3L-BGMs, especially the spin-resolved band structures. The results are summarized in Figs. 5 and 6. Our main findings are (1) First, the spin-up and spin-down bands of the LAF state in the 3L-BGM are no longer degenerate in the zero electric field case. (2) The influence of the vertical electric field on the LAF state in 3L-BGMs is totally different from that in 4L-BGMs. (3) The calculated band structures indicate that the required parameter range to realize a half-metallic phase is much smaller than that in 4L-BGMs, which implies that it is rather hard to observe the half-metallic phase in 3L-BGMs.

In the single-particle picture, the 3L-BGM has a pair of parabolic bands and a pair of linear bands touching at the Dirac point, as shown in the inset of Fig. 5(a). Coulomb interaction is able to induce a LAF state, and the corresponding

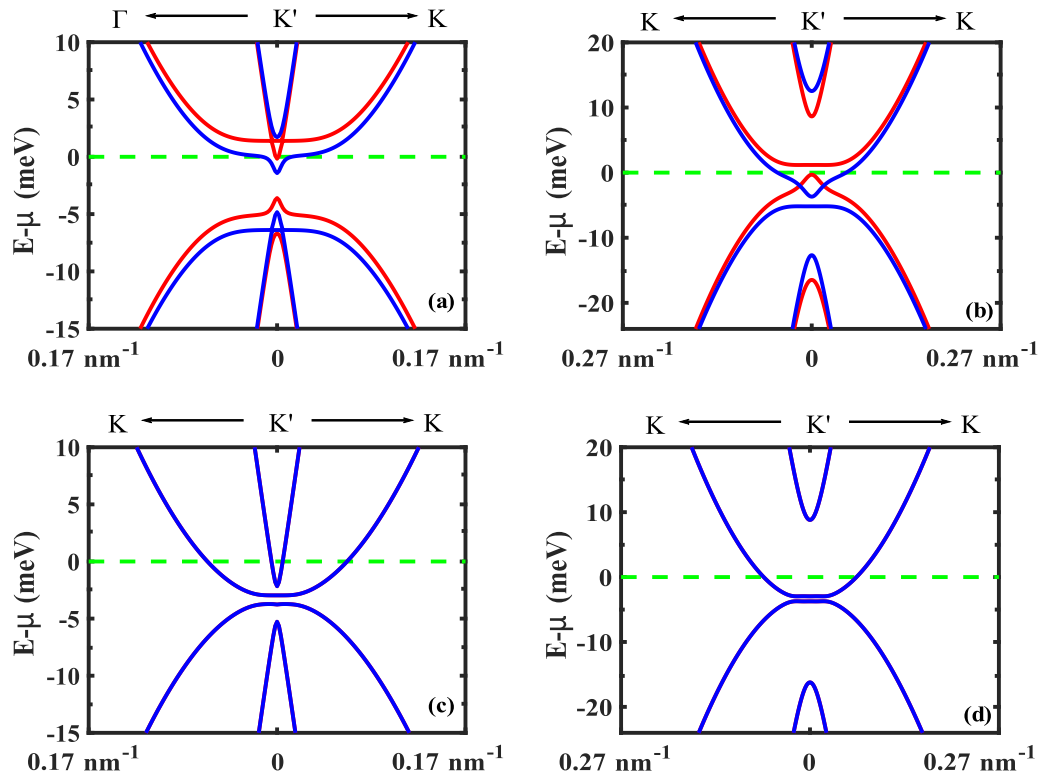

FIG. 6. Half-metallic phases in 3L-BGM. (a) and (b) are the energy bands of the proposed half-metal states with electron density (a) $\delta n \approx 0.34 \times 10^{10}\,\mathrm{cm}^{-2}$ and (b) $\delta n \approx 3.22 \times 10^{10}\,\mathrm{cm}^{-2}$. (c) and (d) show the energy bands of the LCP states with a large charge density (c) $\delta n \approx 1.29 \times 10^{11}\,\mathrm{cm}^{-2}$ and (d) $\delta n \approx 1.26 \times 10^{11}\,\mathrm{cm}^{-2}$. The parameters used in (a) and (c) are the same as that in Fig. 5(c), and the parameters in (b) and (d) are the same as that in Fig. 5(d).

spin-resolved band structure is given in Fig. 5(b). We see that both the linear bands and the parabolic bands are gapped, and the spin structure of the LAF state is shown in Fig. 4(a). The calculated LAF state here is qualitatively in agreement with the DFT calculation. A notable difference is that, as shown in the DFT calculation, the remote hopping will slightly shift the relative position of the linear bands (about 10 meV), which is not included in our model. The shifted linear bands will always contribute a small but finite conductance in the transport measurements, and the pseudogap observed in the experiment should be the gap between the parabolic bands [47]. However, we argue that our model here captures the main characteristics of the LAF state in 3L-BGMs, i.e., the antiferromagnetic spin order and the interaction induced gap. The induced gap ϵ_g, as well as the pseudogap, relies on the U, which is shown in Fig. 5(a). Here, we set $U = 6.70\,\mathrm{eV}$ to fit the observed pseudogap in the experiment, about 5 meV [47].

A remarkable phenomenon in 3L-BGMs is that, in zero electric field, the spin-up and spin-down bands are no longer degenerate [see Fig. 5(b)], where the valence and conduction bands have opposite spin polarizations. It is quite different from the case of 4L-BGMs, and actually results from the special lattice structure of 3L-BGMs. In Fig. 4, we see that 3L-BGMs have an antiferromagnetic spin order as well, where spin-up (spin-down) electrons are mainly on sublattice A (B). Note that sublattice A and sublattice B are inequivalent here. Thus, from the point of the mean field, spin-up and -down electrons feel different potentials, which is different from that in 4L-BGMs. This is the reason why the spin degeneracy of the bands is lifted in 3L-BGMs. This interesting phenomenon further implies that, with two inequivalent sublattices, the Hubbard model can intrinsically give rise to an antiferromagnetic state with spin nondegenerate bands without need of an additional potential to further break the spin degeneracy of the bands, unlike that in ionic Hubbard models [41]. This prediction can be immediately tested in some simple lattice models, e.g., a Lieb lattice.

We then discuss the influence of the vertical electric field E_0. In Fig. 5(c), we apply a small electric field $E_0 = 10\,\mathrm{mV\,nm}^{-1}$. Compared with the zero field case in Fig. 5(b), a small E_0 only slightly modifies the shape of the spin-resolved bands and moves the conduction (valence) band downward (upward). Note that E_0 evidently does not enhance the split between the spin-up and spin-down bands. The effect of E_0 is the same in the large electric field case, as shown in Fig. 5(d) with $E_0 = 80\ \mathrm{mV\,nm}^{-1}$. Here, the valence band (spin up) is shifted upward and the conduction band (spin down) is moved downward further, which gives rise to a negative gap at the Fermi level. Similarly, the split between the spin-up and spin-down bands is still very small. Further calculations indicate that the LAF state in 3L-BGMs is very robust against E_0, where the antiferromagnetic spin order still exists in an extremely large $E_0 = 2\,\mathrm{eV\,nm}^{-1}$. As functions of E_0, the spin polarization of each site is plotted in Fig. 5(e) and the corresponding spin structure is illustrated in Fig. 4(b). The charge variation of each layer is given in Fig. 5(f). We see that the change of spin polarization is very slow when increasing E_0. Meanwhile, as E_0 increases, charges are mainly transferred

from the bottom layer (layer 1) to the top layer (layer 3), while that in the middle layer is nearly invariant.

Though the spin split of the bands is not very large in 3L-BGM, in principle, proper doping can still induce a half-metallic phase. In Fig. 6, we show the induced half-metallic phases in 3L-BGM. In Fig. 6(a), we apply an electric field $E_0 = 10\,\mathrm{meV\,nm^{-1}}$ and a doping $\delta n = 0.34 \times 10^{10}\,\mathrm{cm^{-2}}$. The Fermi level is shifted into the conduction band (spin down), so the spin-down electrons are conducting and the spin-up electrons are still gapped. It thus gives rise to a half metal. In Fig. 6(b), we apply an electric field $E_0 = 80\,\mathrm{meV\,nm^{-1}}$ and a doping $\delta n = 3.22 \times 10^{10}\,\mathrm{cm^{-2}}$. In this case, only spin-down electrons are conducting as well, so it is also a half metal. However, we note that, in both cases, the spin-up bands are very close to the Fermi level. Thus, in reality, it is hard to detect the predicted spin-dependent gap in the transport experiment. In other words, 3L-BGM is not a good platform to realize the half-metallic state. The detectable feature of the half metal in 3L-BGMs may be the nonzero net magnetic moment in the presence of electric field and doping. Since the required doping is of the order of $10^{-10}\,\mathrm{cm^{-2}}$, the doping-induced magnetic moment should be of the order of $10^{-10}\mu_B\,\mathrm{cm^{-2}}$. Note that larger doping will directly kill the LAF states of 3L-BGMs, see Figs. 6(c) and 6(d), where the spin-up and spin-down bands become degenerate.

IV. SUMMARY

We theoretically propose that it is possible to produce a half-metallic phase in BGM systems by applying a vertical electric field and proper doping. Based on the Hubbard model and self-consistent method, we systematically study the correlated ground states of 4L-BGMs and 3L-BGMs in the presence of a vertical electric field and doping, where the 4L-BGM (3L-BGM) is considered a typical example of even-layer (odd-layer) BGMs. Our results show that both the 4L-BGM and 3L-BGM can support a stable LAF state with antiferromagnetic spin order. In 4L-BGMs, a vertical electric field will lift the degeneracy of the spin-up and spin-down bands, and give rise to a spin-dependent gap. Increasing E_0, we find an interesting phenomenon of spin-polarized band inversion, where the spin polarization of the conduction and valence bands are inverted. It is a unique feature of the LAF state in even-layer BGM. Furthermore, a tiny doping can shift the Fermi level into the spin-polarized conduction band (or valence band), which thus gives rise to a half-metallic phase with a nonzero net magnetic moment. The 3L-BGM has different behaviors. Due to its special lattice structure, the spin degeneracy of the bands is lifted even in the zero electric field case. The conduction and valence bands have opposite spin polarization here. As E_0 increases, the gap between the conduction and valence bands decreases and a negative gap can be achieved. However, the split between the spin-up and spin-down bands is always quite small, no matter whether E_0 is applied or not. Thus, though doping can still induce a half-metallic phase like that in 4L-BGMs, we expect that it is hard to detect the half-metallic phase in 3L-BGMs. We note that the antiferromagnetic spin order (LAF state) in 3L-BGMs is very robust against E_0.

From the point of the experiment, we suggest that 4L-BGMs are an ideal platform to detect the proposed half-metallic phase in BGMs. The feasible ways may be to measure the spin-resolved gap or the nonzero net magnetic moment. Finally, we would like to mention that, in two-dimensional (2D) antiferromagnetic systems, vertical electric field-induced half-metallic states should be a general phenomenon, which is found not only in graphene systems but also in other 2D antiferromagnets [62–64].

ACKNOWLEDGMENTS

We acknowledge support from the National Natural Science Foundation of China (Grants No. 11874160, No. 12141401, and No. 11534001), the National Key Research and Development Program of China (No. 2017YFA0403501), the Fundamental Research Funds for the Central Universities (HUST: No. 2017KFYXJJ027), and National Basic Research Program of China (Grant No. 2019YFA0308403).

[1] N. Tombros, C. Jozsa, M. Popinciuc, H. T. Jonkman, and B. V. Wees, Nature (London) **448**, 571 (2007).
[2] B. Dlubak, M. B. Martin, C. Deranlot, B. Servet, S. Xavier, R. Mattana, M. Sprinkle, C. Berger, W. D. Heer, and F. Petroff, Nat. Phys. **8**, 557 (2012).
[3] D. Pesin and A. H. MacDonald, Nat. Mater **11**, 409 (2012).
[4] W. Han, R. K. Kawakami, M. Gmitra, and J. Fabian, Nat. Nanotechnol. **9**, 794 (2014).
[5] Y. Liu, C. Zeng, J. Zhong, J. Ding, Z. M. Wang, and Z. Liu, Nano-Micro Lett. **12**, 93 (2020).
[6] W. Yan, L. C. Phillips, M. Barbone, S. J. Hämäläinen, A. Lombardo, M. Ghidini, X. Moya, F. Maccherozzi, S. van Dijken, S. S. Dhesi, A. C. Ferrari, and N. D. Mathur, Phys. Rev. Lett. **117**, 147201 (2016).
[7] A. H. Castro Neto, F. Guinea, N. M. R. Peres, K. S. Novoselov, and A. K. Geim, Rev. Mod. Phys. **81**, 109 (2009).
[8] S. Das Sarma, S. Adam, E. H. Hwang, and E. Rossi, Rev. Mod. Phys. **83**, 407 (2011).
[9] I. Choudhuri, P. Bhauriyal, and B. Pathak, Chem. Mater. **31**, 8260 (2019).
[10] A. C. Ferrari, F. Bonaccorso, V. Fal'ko, K. S. Novoselov, S. Roche, P. Bøggild, S. Borini, F. H. L. Koppens, V. Palermo, N. Pugno, J. A. Garrido, R. Sordan, A. Bianco, L. Ballerini, M. Prato, E. Lidorikis, J. Kivioja, C. Marinelli, T. Ryhänen, A. Morpurgo *et al.*, Nanoscale **7**, 4598 (2015).
[11] R. A. de Groot, F. M. Mueller, P. G. van Engen, and K. H. J. Buschow, Phys. Rev. Lett. **50**, 2024 (1983).
[12] M. I. Katsnelson, V. Y. Irkhin, L. Chioncel, A. I. Lichtenstein, and R. A. de Groot, Rev. Mod. Phys. **80**, 315 (2008).
[13] Y. Liu and B.-G. Liu, J. Phys. D **40**, 6791 (2007).
[14] K. Yao, G. Gao, Z. Liu, L. Zhu, and Y. Li, Phys. B: Condens. Matter **366**, 62 (2005).
[15] G. Y. Gao and K.-L. Yao, Appl. Phys. Lett. **103**, 232409 (2013).

[16] C. Felser and A. Hirohata, *Heusler Alloys* (Springer, Cham, 2016), Vol. 222.

[17] Y. W. Son, M. L. Cohen, and S. G. Louie, Nature (London) **444**, 347 (2006).

[18] E. J. Kan, Z. Li, J. Yang, and J. G. Hou, Appl. Phys. Lett. **91**, 243116 (2007).

[19] W. Kim and K. Kim, Nat. Nanotechnol. **3**, 408 (2008).

[20] Y. Li, Z. Zhou, P. Shen, and Z. Chen, ACS Nano **3**, 1952 (2009).

[21] M. Wu, X. Wu, Y. Gao, and X. C. Zeng, Appl. Phys. Lett. **94**, 223111 (2009).

[22] J. Yuan, D.-H. Xu, H. Wang, Y. Zhou, J.-H. Gao, and F.-C. Zhang, Phys. Rev. B **88**, 201109(R) (2013).

[23] J. Baima, F. Mauri, and M. Calandra, Phys. Rev. B **98**, 075418 (2018).

[24] A. Szabo and B. Roy, arXiv:2109.04466.

[25] R. A. de Groot, Phys. B: Condens. Matter **172**, 45 (1991).

[26] H. van Leuken and R. A. de Groot, Phys. Rev. Lett. **74**, 1171 (1995).

[27] H. Akai and M. Ogura, Phys. Rev. Lett. **97**, 026401 (2006).

[28] X. Hu, Adv. Mater **24**, 294 (2011).

[29] F. Zhang and A. H. MacDonald, Phys. Rev. Lett. **108**, 186804 (2012).

[30] D.-H. Xu, J. Yuan, Z.-J. Yao, Y. Zhou, J.-H. Gao, and F.-C. Zhang, Phys. Rev. B **86**, 201404(R) (2012).

[31] M. M. Scherer, S. Uebelacker, D. D. Scherer, and C. Honerkamp, Phys. Rev. B **86**, 155415 (2012).

[32] T. C. Lang, Z. Y. Meng, M. M. Scherer, S. Uebelacker, F. F. Assaad, A. Muramatsu, C. Honerkamp, and S. Wessel, Phys. Rev. Lett. **109**, 126402 (2012).

[33] Y. Wang, H. Wang, J.-H. Gao, and F.-C. Zhang, Phys. Rev. B **87**, 195413 (2013).

[34] H. Wang, J.-H. Gao, and F.-C. Zhang, Phys. Rev. B **87**, 155116 (2013).

[35] J. Sun, D.-H. Xu, Y. Zhou, and F.-C. Zhang, Phys. Rev. B **90**, 125429 (2014).

[36] A. Rozhkov, A. Sboychakov, A. Rakhmanov, and F. Nori, Phys. Rep. **648**, 1 (2016).

[37] M. Otani, M. Koshino, Y. Takagi, and S. Okada, Phys. Rev. B **81**, 161403(R) (2010).

[38] F. Zhang, J. Jung, G. A. Fiete, Q. Niu, and A. H. MacDonald, Phys. Rev. Lett. **106**, 156801 (2011).

[39] B. Pamuk, J. Baima, F. Mauri, and M. Calandra, Phys. Rev. B **95**, 075422 (2017).

[40] Y. Lee, D. Tran, K. Myhro, J. Velasco, N. Gillgren, C. N. Lau, Y. Barlas, J. M. Poumirol, D. Smirnov, and F. Guinea, Nat. Commun. **5**, 5656 (2014).

[41] A. Garg, H. R. Krishnamurthy, and M. Randeria, Phys. Rev. Lett. **112**, 106406 (2014).

[42] S. Bag, A. Garg, and H. R. Krishnamurthy, Phys. Rev. B **103**, 155132 (2021).

[43] Y. Lee, S. Che, J. V. Jr., D. Tran, J. Baima, F. Mauri, M. Calandra, M. Bockrath, and C. N. Lau, arXiv:1911.04450.

[44] H. Zhou, T. Xie, A. Ghazaryan, T. Holder, and A. F. Young, Nature (London) **598**, 429 (2021).

[45] Y. Nam, D.-K. Ki, M. Koshino, E. McCann, and A. F. Morpurgo, 2D Mater. **3**, 045014 (2016).

[46] A. L. Grushina, D.-K. Ki, M. Koshino, A. A. L. Nicolet, C. Faugeras, E. McCann, M. Potemski, and A. F. Morpurgo, Nat. Commun. **6**, 6419 (2015).

[47] Y. Nam, D.-K. Ki, D. Soler-Delgado, and A. F. Morpurgo, Science **362**, 324 (2018).

[48] F. Guinea, A. H. Castro Neto, and N. M. R. Peres, Phys. Rev. B **73**, 245426 (2006).

[49] S. Latil and L. Henrard, Phys. Rev. Lett. **97**, 036803 (2006).

[50] B. Partoens and F. M. Peeters, Phys. Rev. B **75**, 193402 (2007).

[51] M. Koshino and T. Ando, Phys. Rev. B **76**, 085425 (2007).

[52] H. Min and A. H. MacDonald, Phys. Rev. B **77**, 155416 (2008).

[53] M. Campetella, J. Baima, N. M. Nguyen, L. Maschio, F. Mauri, and M. Calandra, Phys. Rev. B **101**, 165437 (2020).

[54] R. Yagi, T. Hirahara, R. Ebisuoka, T. Nakasuga, S. Tajima, K. Watanabe, and T. Taniguchi, Sci. Rep. **8**, 13018 (2018).

[55] B. Partoens and F. M. Peeters, Phys. Rev. B **74**, 075404 (2006).

[56] V. O. Özçelik and S. Ciraci, Phys. Rev. B **86**, 155421 (2012).

[57] M. Calzá, A. Casalino, O. Luongo, and L. Sebastiani, Eur. Phys. J. Plus **135**, 1 (2020).

[58] H. Zhou, L. Holleis, Y. Saito, L. Cohen, W. Huynh, C. L. Patterson, F. Yang, T. Taniguchi, K. Watanabe, and A. F. Young, arXiv:2110.11317.

[59] S. C. de la Barrera, S. Aronson, Z. Zheng, K. Watanabe, T. Taniguchi, Q. Ma, P. Jarillo-Herrero, and R. Ashoori, arXiv:2110.13907.

[60] J. Nilsson, A. H. Castro Neto, N. M. R. Peres, and F. Guinea, Phys. Rev. B **73**, 214418 (2006).

[61] H. Liu, H. Jiang, and X. C. Xie, AIP Adv. **2**, 041405 (2012).

[62] S.-J. Gong, C. Gong, Y.-Y. Sun, W.-Y. Tong, C.-G. Duan, J.-H. Chu, and X. Zhang, Proc. Natl. Acad. Sci. USA **115**, 8511 (2018).

[63] P. Jiang, L. Kang, H. Hao, X. Zheng, Z. Zeng, and S. Sanvito, Phys. Rev. B **102**, 245417 (2020).

[64] H. Lv, Y. Niu, X. Wu, and J. Yang, Nano Lett. **21**, 7050 (2021).